Time-dependent wave packet simulations of transport through Aharanov-Bohm rings with an embedded quantum dot

C. Kreisbeck[1], T. Kramer[2,3], R.A. Molina[4]

[1] Department of Chemistry and Chemical Biology, Harvard University, Cambridge, Massachusetts 02138, USA
[2] Zuse Institute Berlin, Berlin, Germany
[3] Department of Physics, Harvard University, Cambridge, Massachusetts 02138, USA
[4] Instituto de Estructura de la Materia - CSIC, 28006 Madrid, Spain

Abstract. We have performed time-dependent wave packet simulations of realistic Aharonov-Bohm (AB) devices with a quantum dot embedded in one of the arms of the interferometer. The AB ring can function as a measurement device for the intrinsic transmission phase through the quantum dot, however, care has to be taken in analyzing the influence of scattering processes in the junctions of the interferometer arms. We consider a harmonic quantum dot and show how the Darwin-Fock spectrum emerges as a unique pattern in the interference fringes of the AB oscillations.

1. Introduction

Interference effects are fundamental for the description of transport in mesoscopic devices. Transport properties of a quantum mechanical system are characterize by the complex transmission coefficient t. The modulus of the transmission coefficient is readily available experimentally by measuring the conductance in a two-terminal configuration. According to the Landauer-Büttiker picture, the conductance for mono-channel leads is proportional to the transmission probability through the system $g = (e^2/h)|t|^2$ [1, 2]. The phase of the transmission coefficient α $(t = |t|e^{i\alpha})$ is, however, a more elusive quantity for experiments.

Phase sensitive experiments were pioneered by Yacoby *et al.* in the 90s [3]. A Quantum Dot (QD) was embedded in one arm of an Aharanov-Bohm (AB) ring. Oscillations in the conductance of the device as a function of the magnetic flux were followed while varying a plunger gate voltage V_g affecting the dot. The relative phase between the pattern of oscillations for different values of V_g would, in principle, depend on the transmission phase of the quantum dot. The device, however, was a two-terminal setup and Onsager relations dictate that the dependence of the conductance of the whole

device has to be an even or odd function of the magnetic flux. Then, the relative phases between the oscillations at different values of V_g can only be 0 or π [2, 4].

A multiple terminal configuration lifts this phase locking condition. Multiterminal devices for extracting the phase information were fabricated by Schuster *at al.* and transmission phases could be extracted from the measured data [5]. The expected Breit-Wigner behavior of the measured transmission phase in each resonance was found, giving credit to the claim of measuring the intrinsic transmission phase of the embedded QD through the analysis of the interference patterns in the conductance of the whole AB device. However, more unexpectedly, the behavior of the phase was the same between all measured resonances. Transmission zeros between every pair of neighboring resonances and the associated π phase lapses were responsible for the in-phase behavior of the sequences of resonances.

This seminal series of works motivated further experiments and a great wealth of theoretical works. On the experimental side, the role of the magnetic field was explored by Sigrist *at al.* in AB ring with one QD embedded in each of its arms [6]. Phase lapses were found for only specific ranges of values of the magnetic field. The phase of a QD in the Kondo regime has also received a lot of attention after Gerland *et al.* predicted that the transmission phase of a QD measured in the AB device should evolve between the π results of Coulomb blockade to the $\pi/2$ result predicted in the Kondo regime depending on temperature and width [7]. The first experiments in the Kondo regime reported a $3\pi/2$ phase shift along the spin-degenerate pair, a surprising result that is still not properly explained [8, 9]. Further experiments claimed to have observed the $\pi/2$ phase shift corresponding to the Kondo regime but the temperature of this experiments was much higher than the Kondo temperature and outside the regime where the Kondo result is expected to hold[10]. More recent experiments by Takada *et al.* have managed to measure the transmission phase shift through a Kondo correlated quantum dot and find the transition between the Kondo regime and Coulomb blockade regime with excellent agreement with Numerical Renormalization Group calculations [11]. Effects of the ratio between width and interaction strength have also been experimentally investigated [12]. Avinun-Kalish *at al.* investigated smaller dots and found the crossover from the universal regime where phase lapses occur in between every neighboring resonance to a mesoscopic regime where phase lapses occur in a random fashion was observed when decreasing the number of electrons from 20 down to 0 [13].

As it became clear, thanks to the work by Levy-Yeyati and Büttiker, phase lapses were associated with zeros in the transmission coefficient, the only situation in which the phase of the complex number as a function of the energy E or as a function of V_g can have a discontinuity [14, 15, 16]. In non-interacting models, zeros of the transmission in the valley between two peaks would appear in between consecutive resonances of the same parity with respect to the lead position[17]. Most of the theoretical works were devoted to the objective of explaining the universal sequences of resonances and phase lapses appearing in experiments [18, 19, 20, 21, 22, 23, 24, 25, 26]. Several works have addressed the importance of the electronic correlations in the transition to the

universal regime [23]. However, many-body numerical calculations have challenged the interpretation of these results [27]. Molina *et al.* found that wavefunction correlations in chaotic ballistic quantum dots could be responsible for the crossover between the mesoscopic regime and universal regime [26]. A more detailed statistical analysis have investigated the stability of the chaotic correlations under the influence of fluctuations [28]. New experiments with a more systematic statistical analysis of the results are needed to discriminate between different theoretical approaches trying to explain the experimental transition between the mesoscopic and the universal regimes.

A different range of theoretical works have tried to analyze up to what extend the experimental results can be trusted to give unambiguous information about the intrinsic transmission phase of the quantum dot. Taking into account the different harmonics due to multiple turns around the AB ring the conductance of the whole device can be written as

$$g = g_0 + \sum_n g_g \cos\left(2\pi n\phi/\phi_0 + \beta_n\right), \tag{1}$$

with the quantum flux ϕ_0. The connection between the measured phase of the conductance oscillations β_1 and the transmission phase α was discussed in several works [16, 29, 30, 31, 32]. The conclusion that could be extracted from these series of works was that under not too restrictive constraints regarding the coupling to the environment the transmission phase α can be extracted from β_1 in multiterminal geometries. However, the main focus was in the opening of the systems and in partial coherent transport using one-dimensional models for the leads without taking into account other distorting effects like possible scattering in the junctions of the interferometric arms. Experimental advances in this direction have been made recently trying to find more clear criteria about when the phase measurements can be trusted and when the contributions from multiple path can be neglected[33].

A different approach was taken by Fischer *et* al. [34]. The purpose was to make very controllable experiments that could be verified by theoretical simulations. They wanted to understand the behavior of the complete device taking into account the two-dimensional character of waveguides and scattering effects due to the junctions and in the leads [35]. The experiments and theoretical calculations in pure AB rings demonstrated the strong influence of scattering effects in the junctions and arms of the ring that were by themselves the sources of phase jumps in the pattern of conductance oscillations as a function of the magnetic field.

The aim of this work is to study the functioning of a realistic four terminal AB device as a phase detector of an embedded quantum dot. For this purpose we use time-dependent wave packet simulations [35, 38] of the whole device from which we extract the complex transmission at different energies from a single run. For our simulations we use a variation of the device fabricated by Fischer *et* al. [34] including a harmonic dot in one of the arms of the interferometer. Using this configuration has several advantages: it has been shown to be experimentally feasible and the pure interferometer without dot has been theoretically modeled before [35, 39]. Due to the size of the dot we take into

account the full effect of the magnetic field and cyclotron orbits inside the dot. Although, scattering effects in the cross-junctions of the device can distort the measurement, careful simulations of the device without dot allow us to predict scattering free regions where the intrinsic dot transmission phase can be extracted from the measurements. The simulations show Zeeman cat's whiskers appearing in the AB oscillation pattern of the device as a signature of the Darwin-Fock spectrum of the dot. As resonances in a Zeeman multiplet have the same parity, phase lapses appear in between all resonances which allow us to identify the quantum numbers corresponding to each resonant peak and use the device for simultaneous phase detection and transport spectroscopy.

The remainder of the manuscript is organized as follows. In Section 2 we outline the used theoretical model and methodology. We summarize the transmission properties of the embedded quantum dot defined by the Darwin-Fock spectrum in Section 3. After that, we demonstrate in Section 4 that the AB-ring geometry can be configured as transmission phase detector of an embedded quantum dot. We show that the Darwin-Fock spectrum emerges as unique patterns in the AB interference fringes.

2. Methodology

A sketch of the setup including information on the parameters used in our simulations is given in the top panel of Fig. 1. The design is based on the experimental device without QD used in Ref. [35]. This allow us to easily compare between results for the device without QD and for the device with QD and to guide the design and fabrication of a real device. A similar design has also been used for mode filtering [40] which can be necessary for a clean measurement of the transmission phase. The experimental rings were fabricated in AlGaAs/GaAs heterostructures. The mean-free path $\ell_e \sim 8-15\ \mu$m is larger than the size of the device geometry. The waveguide had radii of $0.5-1\ \mu$m. This ensures coherent electron transport along the ring and minimizes scattering at impurities and inelastic scattering. Similar experimental devices and theoretical techniques have been used to study thermal currents [39].

We use the effective mass approximation and describe the electron transport in terms of a single particle picture. The effective mass for the AlGaAs/GaAs heterostructure is given by $m^* = 0.067 m_e$, where m_e stands for the electron mass. The magnetic field is included by minimal coupling replacing $\mathbf{p} \to -i\hbar\nabla + e\mathbf{A}(x,y)$. We describe the electron transport within the ballistic regime and interpret the experimental outcome in terms of elastic scattering. We compute the transmission amplitudes with a time-dependent wave-packet approach. The basic ideas for the application of the wave-packet approach to mesoscopic physics are given in Ref. [36, 37, 38]. The time-dependent approach is based on wave-packet propagation. While the transversal shape of the wave packets is governed by the harmonic confinement of the asymptotic leads, we are free to choose the longitudinal component. In the following, we use Gaussian wave packets. The time-dependent approach has several advantages: (i) the quantum choreography of the propagated pulse gives an intuitive physical picture of the scattering
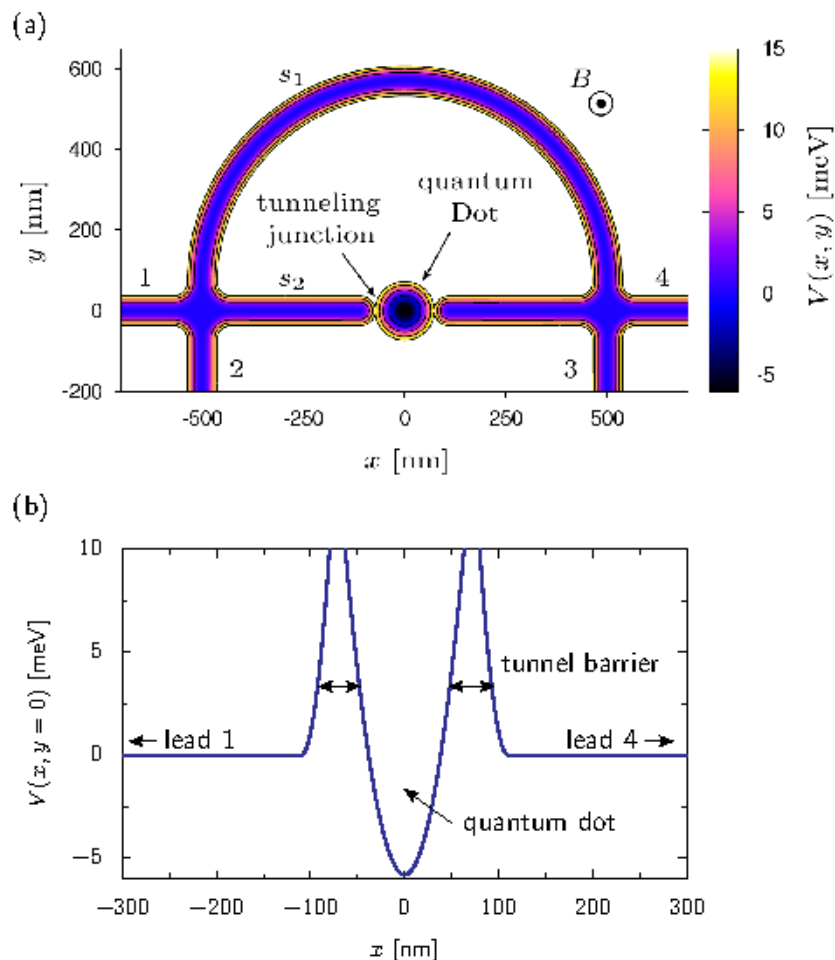
Figure 1. (a) Potential landscape of the AB interferometer configured as a transmission phase detector of an embedded quantum dot. The ring is constructed in the same way as in [35]. We assume an isotropic harmonic quantum dot. (b) shows a cut in x-direction of the potential along the center of the lower arm s_2 of the ring (y=0). We configure the quantum dot into the resonant tunneling regime. The distance between the caps and the center of the quantum dot adjusts the tunneling coupling. We use a distance of 110 nm.

mechanisms involved in the transfer process, (ii) the wave packet propagation efficiently computes the energy resolved transmission amplitudes for a large range of energies, and (iii) a time-dependent approach allows us to simulate general multi-terminal devices with complicated geometries and topologies. More details of the simulation and snapshots of the time evolution can be found in the Appendix.

In order to perform realistic simulations we incorporate the 2d potential landscape (see Fig. 1). Although the whole procedure is within a non-interacting particle picture, the potential landscape in the leads and in the quantum dot effectively take into account depletion effects due to Coulomb interaction. Other effects of the Coulomb interaction like the charging energy of the dot and effects of strong correlations beyond mean field are not taken into account in our approach. We expect charging effects in the dot to

separate the levels in energy essentially without modifying the phase information in the measurements. The asymptotic leads are given as harmonic waveguides with a confining frequency $\hbar\omega = 5$ meV. We accurately model the junctions as rounded orthogonal cross-junctions ($R_{\text{junction}} = 70$ nm). The latter induce collimation effects that significantly change the scattering behavior [41]. We set the radius of the ring to $R = 0.5~\mu$m. To avoid phase locking due to device symmetries [35], we configure the four-terminal device in the non-local setup, in which voltage and current probes are spatially separated. In this configuration the current I_{43} flows between lead 3 and lead 4, while the voltage drop V_{12} is detected at lead 1 and lead 2. We define the non-local resistance

$$R_{43,12} = \frac{V_{12}}{I_{43}}. \tag{2}$$

To avoid disturbing multi-mode effects, we configure the interferometer into a transport regime where only two open modes contribute to the transport. A mode-filtered electron injection allows experimentalists to perform even single-mode transport in a multi-mode waveguide structure [40]. Visualization of the transmission phase of the embedded quantum dot requires a continuous phase drift of the AB oscillations while scanning through the Fermi energy [13]. Since already the empty device shows complicated effects [34, 35, 42], a suitable and careful preparation of the setup is required. Reflection in the junctions and standing waves in the arms lead to resonances and non-trivial scattering effects. Those show for example as phase lapses in the AB interference fringes [35]. In our simulations (linear regime), see upper panel in Fig. 2, there is a distorted region in the interference pattern for Fermi energies in the range between 8.8 meV and 9.1 meV. Therefore, we carefully adjust the range of the Fermi energy under consideration. There is a well-defined continuous phase drift for Fermi energies in the range between 9.1 meV to 9.5 meV. Experimentally, the relevant Fermi energy range can be adjusted by applying a local gate voltage [5, 13] to shift the energy-levels of the quantum dot relative to the leads and the AB ring.
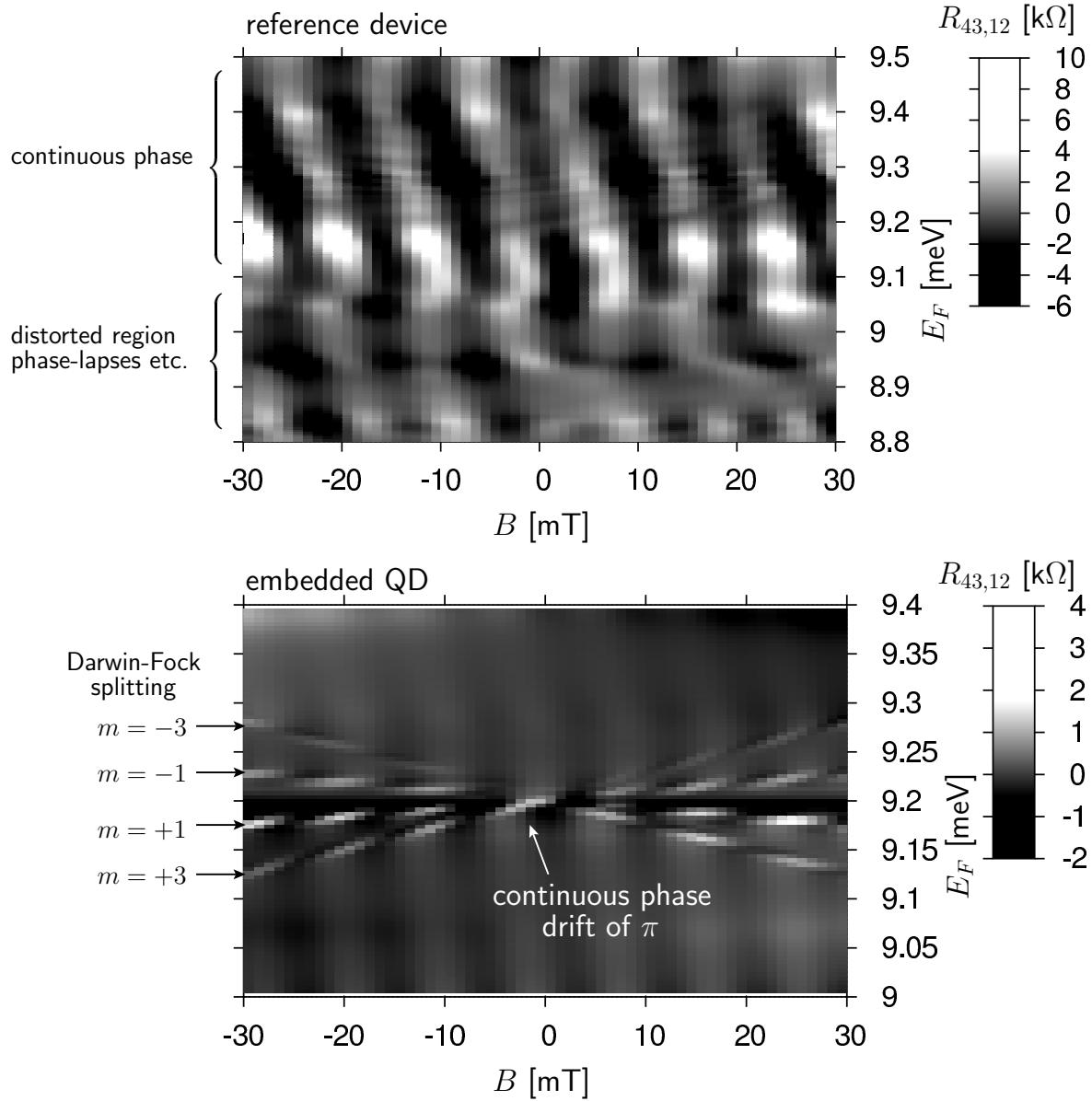
3. Darwin-Fock spectrum

First we consider a two-terminal configuration and calculate the transmission of the harmonic quantum dot embedded in the waveguide s_2. The potential of the harmonic quantum dot is given by (up to some energy, see bottom panel of Fig. 1)

$$V_{\text{dot}} = \frac{1}{2}m^*\omega_{\text{dot}}^2(x^2 + y^2) + V_g, \tag{3}$$

where $\hbar\omega_{\text{dot}}$ is the harmonic frequency and V_g models the influence of the local gate-voltage. The energy levels of the harmonic quantum dot are given by the Darwin-Fock spectrum [43]

$$E_{n,m} = (n+1)\hbar\Omega + \frac{1}{2}\hbar\omega_c m + V_g, \quad \text{with} \quad \Omega = \sqrt{\omega^2 + \frac{\omega_c^2}{4}}, \tag{4}$$

with $\omega_c = eB/m^*$. For the weak applied magnetic fields we neglect the Zeeman spin splitting. The main quantum number is defined by n, while m denotes the $n+1$ angular

reference device

$R_{43,12}$ [kΩ]

continuous phase

distorted region
phase-lapses etc.

E_F [meV]

B [mT]

embedded QD

$R_{43,12}$ [kΩ]

Darwin-Fock
splitting

$m = -3$

$m = -1$

$m = +1$

$m = +3$

continuous phase
drift of π

E_F [meV]

B [mT]

Figure 2. Gray-scale plot of the oscillatory component of the resistance $R_{43,12}$ as a function of the magnetic field and the Fermi energy. Upper panel: AB interference fringes for the reference device (4-terminal ring without embedded quantum dot). Lower panel: AB interferometer configured as transmission phase detector. The potential $V_g = -5.8$ meV is adjusted in such a way that the quantum number $n = 3$ of the Darwin-Fock spectrum is around $E_F = 9.2$ meV, a region for which the reference device shows a clean phase-drift. The Darwin-Fock spectrum induces a splitting of the angular momentum states with an increasing magnetic field and induces *cat's whisker* like interference fringes.

momentum states with $m = -n, -n+2, ..., n$. The eigenstates in polar coordinates

(a)

(b)
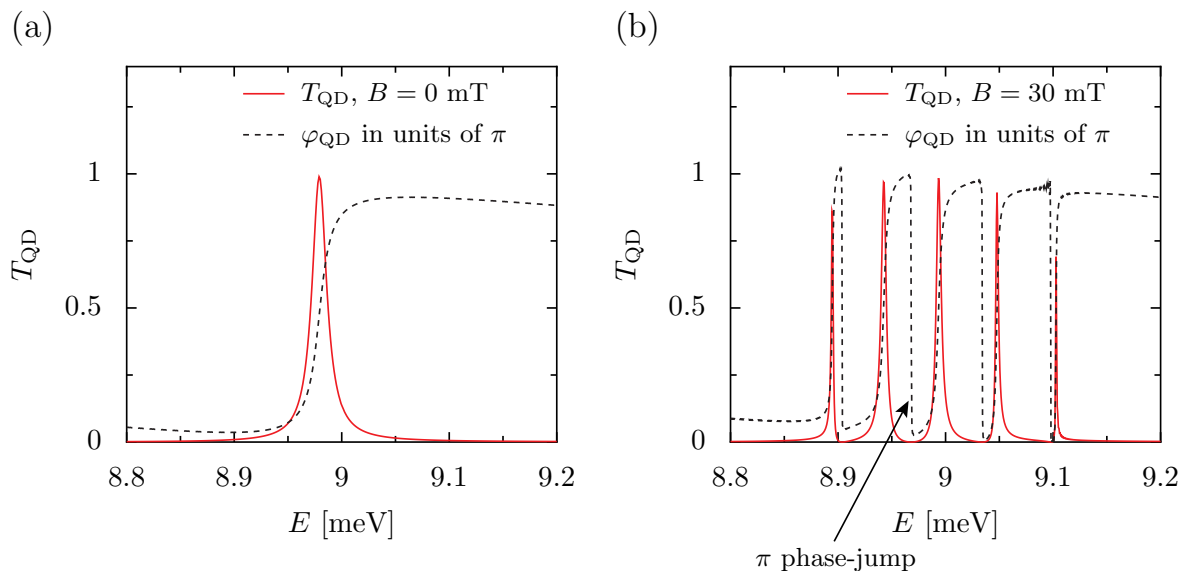
Figure 3. Transmission amplitude $T_{\rm QD}=|t_{\rm QD}e^{i\varphi_{\rm QD}}|^2$ as function of the Fermi energy in a two-terminal resonant tunneling setup. The dashed line corresponds to the transmission phase $\varphi_{\rm QD}$ in units of π. Shown is the corresponding Darwin-Fock spectrum for the quantum number $n=4$ ($V_g = -6$ meV, $\hbar\omega_{\rm dot} = 3$ meV) for (a) $B = 0$ mT and (b) $B = 30$ mT.

read

$$\Phi_{n_r,m}(\mathbf{r}) = \frac{1}{\sqrt{2\pi}}e^{im\phi}\frac{1}{l_0}\sqrt{\frac{n_r!}{(n_r+|m|)!}}\,e^{-r^2/4l_0^2}\left(\frac{r}{\sqrt{2}l_0}\right)^{|m|}L_{n_r}^{|m|}(r^2/2l_0^2), \quad (5)$$

with radial quantum number $n_r = (n-|m|)/2$ and $l_0 = \sqrt{\hbar/m^*\Omega}$. $L_{n_r}^{|m|}$ are the generalized Laguerre polynomials.

Fig. 3 charts the transmission probability $T_{\rm QD}=|t_{\rm QD}e^{i\varphi_{\rm QD}}|^2$ and the transmission phase $\varphi_{\rm QD}$ as functions of the Fermi energy E_F. Without the magnetic field, $B = 0$ mT (Fig. 3(a)), the angular momentum states m of the harmonic oscillator are degenerate. The transmission probability $T_{\rm QD}$ for transport through the quantum dot shows a Breit-Wigner resonance around Fermi energy $E_F = 9$ meV, corresponding to the oscillator state with quantum number $n = 4$ ($V_g = -6$ meV, $\hbar\omega_{\rm dot} = 3$ meV). There is a slight shift of the resonance to lower energies due to the influence of the tunneling junctions. The transmission phase $\phi_{\rm QD}$ changes continuously by π, while scanning the Fermi energy E_F through the resonance. This is expected from the Breit-Wigner shape and is consistent with the Friedel sum rule. The width of the resonance depends on the strength of the tunneling coupling.

The situation is different for a finite magnetic field. Here, the degeneracy of the angular momentum m is lifted, and the single resonance splits into $n+1$ angular states, as is illustrated in Fig. 3(b). All angular momentum states exhibit the same parity. As a consequence the transmission probability $T_{\rm QD}$ drops to zero between each resonance. Thus, the continuous phase drift of π at each resonance is interrupted by an abrupt π

phase-jump. Note that in very high magnetic fields when the different Zeeman multiplets mix this is no longer the case. In general, it is expected that zeros in the transmission disappear for finite magnetic fields and the partial widths of the different states of the dot become complex numbers [44]. However, for harmonic dots connected symmetrically to the leads this is not the case because of the conservation of parity in the Darwin-Fock eigenstates of the open dot.

A more realistic description of the electronic states in the dot should include charging energy effects that lead to Coulomb blockade peaks. A simple but very succesful model for including these effects it the constant interaction (CI) model. Within the constant interaction model the peaks are separated by the charging energy of the dot e/C where C is the dot's capacitance. The modifications of the Darwin-Fock spectrum in the CI model are well known [45] and can describe experimental data in a wide range of parameters [46]. Parity properties of the states are not modified in the CI model and phase behavior should be identical to our description in the following section. The corrections induced by the CI model to the Darwin-Fock spectrum depend on the ration between charging energy and frequency of the harmonic potential. The typical values of the charging energy for the geometry we have used in GaAs quantum dots is 0.3 meV which is an order the magnitude smaller than the frequency of the potential $\hbar\omega_{\mathrm{dot}} = 3$ meV [47]. For ratios similar to this, the measured results in spectroscopic experiments coincide with the expected from the Darwin-Fock spectrum with only small deviations due to interactions or asymmetries in the dot [48, **?**].

4. Zeeman transport spectroscopy

The transmission phase information is encoded in the interference fringes of the AB oscillations of the four-terminal measurement. We place the quantum dot in arm s_2 and run the simulations for the potential landscape depicted in Fig. 1(b). We adjust V_g such that the resonance $n = 3$ of the quantum dot is located in a region for which the empty device shows a clean phase drift. Here we set $V_g = -5.8$ meV. We evaluate the non-local resistance $R_{43,12}$ in the linear regime (see Appendix C). The lower panel in Fig. 2 depicts the oscillatory component of $R_{43,12}$ as function of the magnetic field and the Fermi energy E_F. The AB interference emerges when the Fermi energy fulfills the condition for resonant tunneling. Only in this situation, both arms contribute to transfer. Since the lowest transversal mode carries sufficient kinetic energy to break the tunneling regime there are minor AB oscillations for off-resonant regions. This is a specific feature of the harmonically capped wave-guides for which the tunneling barrier closes with increasing longitudinal energy.

The splitting of the angular momentum states m with increasing magnetic field B is nicely visible in the oscillatory component of $R_{43,12}(B)$ as a function of the Fermi energy. In the AB interference fringes there emerge four lines reflecting the angular momentum states. The zeros in the transmission amplitude and the accompanied phase jumps of π create the unique *cat's whisker* like pattern in the non-local resistance $R_{43,12}$.

For small magnetic fields $|B| \approx 5$ mT, the resonances of the angular momentum overlap with each other to form a single broad resonance that shows a continuous phase drift of π.

5. Conclusions

For a realistic AB electron interferometer we have performed time-dependent wave-packet simulations to analyze under which conditions the device can be used as for measurements of the transmission phase of an embedded quantum dot. Controlling the properties of the device we find certain range of parameters that avoid scattering in the junctions and arms of the interferometer allowing the use of the device for phase measurement. We have studied an example of a harmonic quantum dot in the presence of magnetic field showing a Darwin-Fock-Darwin spectrum. The pattern of conductance oscillations as a function of the magnetic field shows characteristic Zeeman cat's whiskers that can be used experimentally for simultaneous transport and phase spectroscopy. In the Zeeman regime, transmission zeros and phase lapses appear in between the different resonances forming the same multiplet as a signature of the same parity of the corresponding Darwin-Fock eigenstates. This is due to the high symmetry of these states and in contrast to the general behavior of the phase lapses that are expected to disappear in the presence of a magnetic field. We believe that our realistic simulations are an important contribution to the understanding of the conditions under which AB interferometers can be used as transport and phase measurement devices. Similar simulations could serve as a guidance for the calibration of such a device. Experimental deviations from the simulation results could be used as experimental signatures of interaction effects.

6. Acknowledgments

Appendix A. Wave-packet propagation and transmission amplitudes

In the ballistic transport regime the total system is composed of a microscopic scattering region (AB ring with embedded QD) that is coupled to macroscopic contacts via semi-infinite leads. That is the total Hamiltonian

$$\mathcal{H} = \sum_i \mathcal{H}_i^{\text{asym}} + \mathcal{H}^{\text{scat}} \tag{A.1}$$

splits into asymptotic parts $\mathcal{H}_i^{\mathrm{asym}}$, describing the leads and a scattering part $\mathcal{H}^{\mathrm{scat}}$. The leads are semi-infinite quasi one-dimensional objects that are quantized in transversal direction. We use a time-dependent approach based on wave packet propagation [38, 49, 50] to compute the transmission amplitude t_{in_i,jn_j}, which corresponds to the probability amplitude of scattering from lead j populating transversal mode n_j to lead i populating transversal mode n_i. Within the Landauer-Büttiker formalism, the microscopic current in each lead is related to the transmission $T_{i,j} = \sum_{n_i,n_j} |t_{in_i,jn_j}|^2$ by

$$I_i = \frac{e}{h} \int \mathrm{d}E \sum_j T_{i,j}(E)(f_i(E) - f_j(E)). \tag{A.2}$$

Here, $f_i(E) = (\exp(E - \mu_i)/k_B T + 1)^{-1}$ describe the Fermi-Dirac distribution for each lead with chemical potential μ_i.

The scattering eigenstates of the full Hamiltonian can be identified with the corresponding eigenstates of the asymptotic leads

$$\mathcal{H}_i^{\mathrm{asym}} \ \psi_{i,n_i,\pm}(E) = E \ \psi_{i,n_i,\pm}(E) \tag{A.3}$$

with

$$E = \frac{\hbar^2 k_i^2}{2m^*} + E_{i,n_i,\pm k_i} \tag{A.4}$$

and

$$\psi_{i,n_i,\pm}(E) = \left(\frac{\partial E}{\partial k_i}\right)^{-\frac{1}{2}} \chi_{i,n_i,\pm k_i} \, e^{\pm \mathrm{i}\, k_i x_i}. \tag{A.5}$$

Here, $\chi_{i,n_i,\pm k_i}$ is the n_i-th transversal mode of lead i with transversal energy $E_{i,n_i,\pm k_i}$. The remaining energy goes into the longitudinal kinetic energy part $E_{\mathrm{kin}} = \hbar^2 k_i^2/2m^*$. The longitudinal orientation of the leads points along coordinate $\hat{x}_i$. Positive longitudinal wave vectors k_i correspond to incoming waves. In the presence of a magnetic field, the transversal modes depend on the longitudinal momentum.

In our simulations the eigenstates in the asymptotic leads $\chi_{i,n_i,\pm k_i} \, e^{\pm \mathrm{i}\, k_i x_i}$ satisfy the normalization condition $\langle \chi_{i,n_i,\pm k_i} \, e^{\pm \mathrm{i}\, k_i x_i} | \chi_{i,n'_i,\pm k'_i} \, e^{\pm \mathrm{i}\, k'_i x_i} \rangle = \delta(k_i - k'_i)\delta_{n_i,n'_i,\pm,\pm}$. Therefore, we need to introduce the factor $(\partial E/\partial k_i)^{-\frac{1}{2}}$ in eq. (A.5) to ensures the normalization condition in 'energy space'

$$\langle \psi_{i,n,\pm}(E) | \psi_{i,n',\pm}(E') \rangle = \delta_{nn',\pm\pm}\delta(E - E'). \tag{A.6}$$

The asymptotic eigenfunctions form a complete orthonormal set in lead i.

Scattering eigenstates of the total Hamiltonian are solutions of the Schrödinger equation that is restricted to the asymptotic regions. We define

$$\mathcal{H} \, \psi_{i,n_i}^{\pm}(E) = \left(\frac{\hbar^2 k_i^2}{2m^*} + E_{i,n_i,\pm k_i}\right) \psi_{i,n_i}^{\pm}(E) = E \, \psi_{i,n_i}^{\pm}(E), \tag{A.7}$$

where $\psi_{i,n_i}^{\pm}(E)$ is related to the asymptotic eigenstates $\psi_{i,n_i,\pm}(E)$ of lead i. In the corresponding time picture, $\psi_{i,n}^{+}$ starts with an incoming wave in lead i with fixed momentum k_i populating transversal mode n_i. After the wave hits the scattering region

(a)

(b)

(c)

(d)
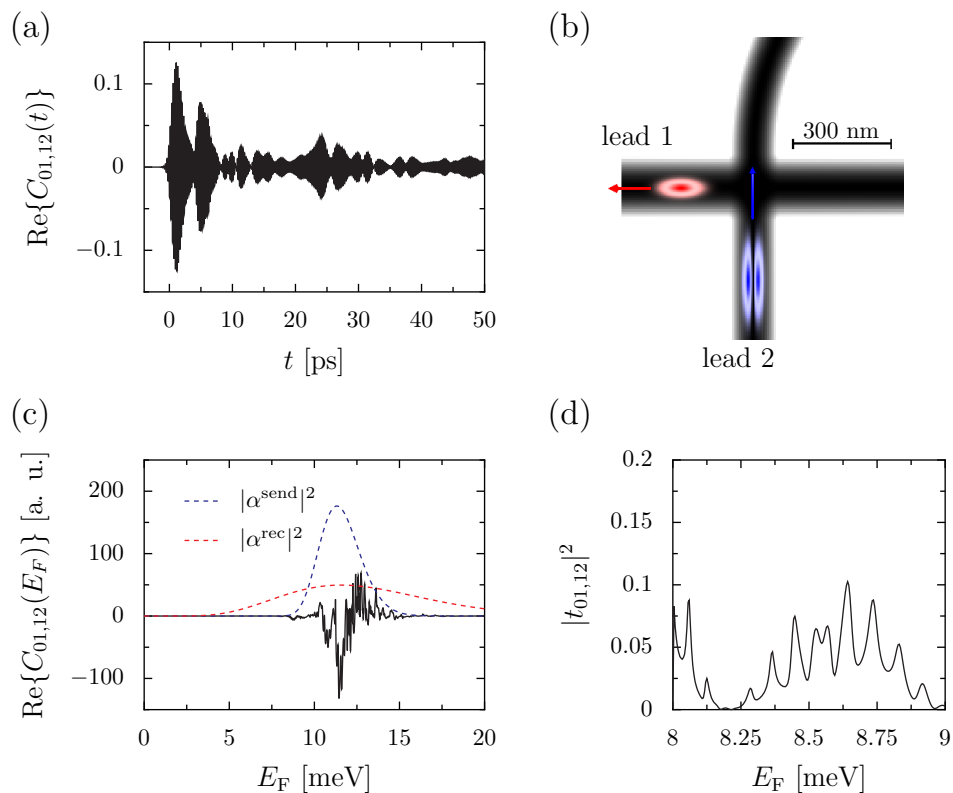
Figure A1. Illustration of the steps involved in the wave-packet approach to get the transmission probability $|t_{01,12}|^2$ for the device geometry shown in Fig. 1 in the main text. (a) time correlation function. (b) visualizes the spatial extension of the receiver (red) and sender (t=0 ps) (blue) wave-packet. (c) real part of the energy representation of the cross-correlation function in arbitrary units. The dashed lines correspond to the energy density of the receiver $|\alpha^{\mathrm{rec}}|^2$ (red) and sender $|\alpha^{\mathrm{send}}|^2$ (blue) wave packet. (d) transmission probability $|t_{01,12}|^2$ calculated according to eq. (A.14).

it gets either reflected in lead i or transmitted to outgoing waves in other asymptotic leads $j \neq i$. Due to inter-mode scattering, the reflected and transmitted parts are superpositions of different transversal modes. The scattering eigenstates ψ^-_{i,n_i} correspond to the time-reversed situation

$$\psi^-_{i,n_i}(B) = \left(\psi^+_{i,n_i}(-B)\right)^*. \tag{A.8}$$

All scattered parts unify in a single outgoing wave with wave vector k_i and transversal mode n_i. $\psi^+_{i,n}$ describes the history, whereas $\psi^-_{i,n}$ describes the destiny of the states. This gives an intuitive picture of the definition of the scattering matrix

$$t_{in_i,jn_j}(E)\delta(E - E') = \langle \psi^-_{i,n_i}(E)|\psi^+_{j,n_j}(E')\rangle, \tag{A.9}$$

which can be interpreted as the projection of the *destiny* on the *history*.

In the following, we establish the concepts behind the wave-packet approach. Let us define an incoming sender wave packet which is is located in one of the asymptotic leads where it populates a specific transversal mode. Moreover, it is composed of purely

incoming longitudinal momenta. Thus the sender wave-packet is represented in terms of scattering eigenstates $\psi_{j,n}^{+}(E)$,

$$\phi_{j,n_j}^{\text{send}} = \int dE \, \alpha_{j,n_j}^{\text{send}}(E) \, \psi_{j,n_j}^{+}(E). \tag{A.10}$$

In an analogous manner, we define a receiver wave-packet that is located in lead i where it populates transversal mode n_i, and is composed of purely outgoing longitudinal momenta,

$$\phi_{i,n_i}^{\text{rec}} = \int dE \, \alpha_{i,n_i}^{\text{rec}}(E) \, \psi_{i,n_i}^{-}(E). \tag{A.11}$$

The receiver represents the destiny of the scattered wave and can be interpreted as a detector. The scattering eigenstates are recovered by

$$\psi_{i,n_i}^{\pm}(E) = \frac{(2\pi\hbar)^{-1}}{\alpha_{i,n_i}^{\text{send/rec}}(E)} \int_{-\infty}^{\infty} dt \, \phi_{i,n_i}^{\text{send/rec}}(t) \, e^{iEt/\hbar}, \tag{A.12}$$

where

$$\phi_{i,n}^{\text{send/rec}}(t) = e^{-i\mathcal{H}t/\hbar} \, \phi_{i,n}^{\text{send/rec}}(t_0 = 0) \tag{A.13}$$

corresponds to the time evolution of the wave packets. During the propagation of the wave packet, it successively traverses the potential landscape and its time-correlation function recovers the stationary solutions of the underlying Hamiltonian. We insert eq. (A.12) into the definition of the scattering matrix eq. (A.9) and recover the transmission amplitudes

$$t_{in_i,jn_j}(E) = \frac{(2\pi\hbar)^{-1}}{(\alpha_{i,n_i}^{\text{rec}}(E))^{*} \, \alpha_{j,n_j}^{\text{send}}(E)} \int_{-\infty}^{\infty} dt \, C_{in_i,jn_j}(t) e^{iEt/\hbar} \tag{A.14}$$

in terms of the cross-correlation function

$$C_{in_i,jn_j}(t) = \langle \phi_{i,n_i}^{\text{rec}} | e^{i\mathcal{H}t/\hbar} | \phi_{j,n_j}^{\text{send}} \rangle = \langle \phi_{i,n_i}^{\text{rec}} | \phi_{j,n_j}^{\text{send}}(t) \rangle. \tag{A.15}$$

The factors $\alpha_{i,n}^{\text{send/rec}}$ depend on the specific shape of the used wave packets

$$\alpha_{i,n_i}^{\text{send/rec}}(E) = \langle \psi_{i,n_i}^{+/-}(E) | \phi_{i,n_i}^{\text{send/rec}} \rangle. \tag{A.16}$$

Since the wave packets $\phi_{i,n_i}^{\text{send/rec}}$ are located in the asymptotic channels, the scattering eigenstates are associated with lead eigenstates. Thus eq. (A.16) reduces to

$$\alpha_{i,n_i}^{\text{send/rec}}(E) = \left(\frac{\partial E}{\partial k_i}\right)^{-\frac{1}{2}} \langle \chi_{i,n_i,\pm k_i} \, e^{\pm i \, k_i x_i} | \phi_{i,n_i}^{\text{send/rec}} \rangle. \tag{A.17}$$

Appendix B. Wave-packet evolution in the embedded dot configuration

In the following we apply the wave-package approach to the four-terminal AB ring with the embedded quantum dot. As illustrative example, we compute the transmission amplitude $t_{10,21}(E)$ for inter-mode scattering from transversal mode 1 in lead 2 to transversal mode 0 in lead 1. The corresponding receiver and sender wave-packets are illustrated in Fig. A1(b). During the propagation of the sender wave-packet,
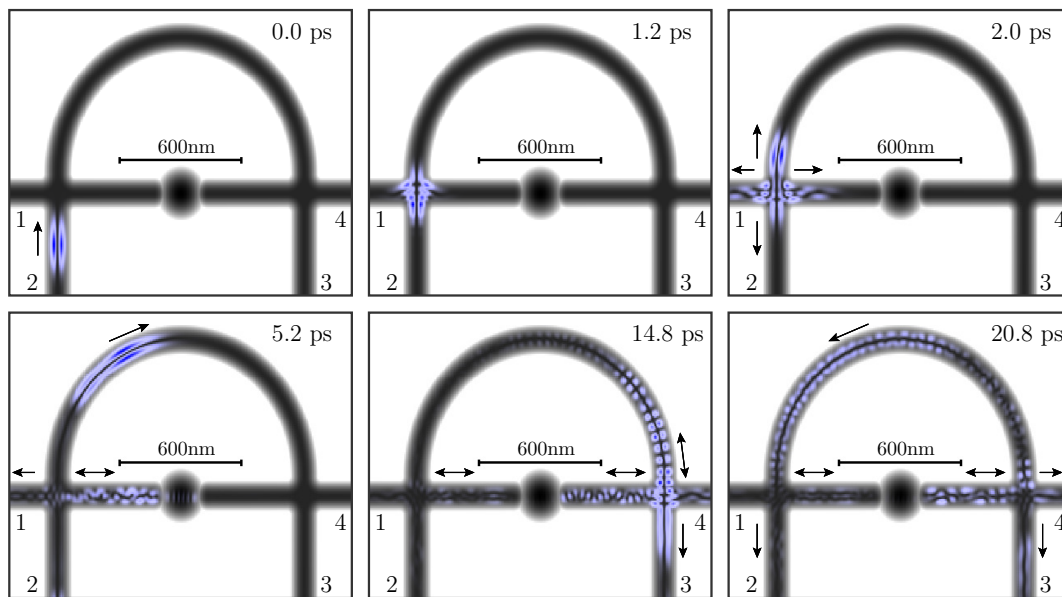
Figure B1. Snapshots of the wave packet propagation. The color (blue) encodes the amplitude of the wave packet. During the time evolution, the wave undergoes multiple scattering events. The arrows indicate the motion of the scattered parts.

we keep track of the cross-correlation function $C_{10,21}(t)$ defined in eq. (A.15). The cross-correlation function reflects the choreography of the wave packet and shows rich structures such as revivals in amplitude, see Fig. A1(a). We perform the Fourier-transform (Fig. A1(c)) and follow eq. (A.14) to obtain the transmission probability $|t_{10,21}(E)|^2$ depicted in Fig. A1(d).

Fig. B1 shows snapshots of the time evolution of the sender wave-packet. The arrows indicate the motion of the wave packet components. The propagation is done with the split-operator method [51]. Initially (0.0 ps), the sender is located in the asymptotic lead 2 and propagates toward the left cross-junction. At 1.2 ps, the sender approaches the center of the junction, scatters in different directions and splits into four parts as is illustrated in the snapshot at 2.0 ps. Some parts get reflected into an outgoing wave in lead 2. Other parts scatter to lead 1 and are detected by the receiver wave-packet. This leads to the large amplitude in $C_{01,12}(t)$ (see Fig. A1(a)) for the time interval between 1 ps and 3 ps. The remaining parts scatter either to the upper arm s_1 or to the lower arm s_2 of the ring. These parts travel along the ring toward the right cross-junction. The lower arm s_1 contains the embedded quantum dot and only few parts of the wave packet that fulfill the conditions for resonant tunneling are transmitted to the right cross-junction. The parts that get reflected at the QD undergo multiple scattering at the left part of the lower arm (see snapshot 5.2 ps), and finally are transferred to lead 1. This process is responsible for the first revival seen in the cross-correlation function around 5 ps – 7 ps. At about 14.8 ps the dominant part of the wave packet traveling along the upper arm of the ring reaches the right-cross junction. Some parts get reflected and go back along the upper arm until they reach again the

left junction at around 20.8 ps.

Appendix C. Evaluation of the non-local resistance in the linear transport regime

According to the Landauer-Büttiker formalism [1, 2], the microscopic currents in each lead of the four terminal AB interferometer are given by eq. (A.2). In the following we consider the linear transport regime, for which we assume that the transport window opened by the difference in the Fermi functions in eq. (A.2) is smaller than the energy scale of fluctuations in the transmission amplitudes $t_{in_i,jn_j}(E)$ (obtained from eq. (A.14)). The microscopic currents are then expressed by linear equations

$$I_i = \frac{e}{h}\left((1 - T_{ii}(E_F)\mu_i - \sum_{j\neq i} T_{ij}(E_F)\mu_j\right), \text{with } T_{i,j} = \sum_{n_i,n_j} |t_{in_i,jn_j}|^2 \quad (C.1)$$

and the local resistance $R_{43,12}$ can be evaluated analytically [2]

$$R_{43,12}(E_F) = \frac{h}{e^2}\frac{T_{14}(E_F)T_{23}(E_F) - T_{13}(E_F)T_{24}(E_F)}{D(E_F)} \quad (C.2)$$

with

$$D(E) = \frac{h^2}{e^4}(\alpha_{11}(E)\alpha_{22}(E) - \alpha_{12}(E)\alpha_{21}(E))S(E)$$

$$\alpha_{11}(E) = \frac{e^2}{hS(E)}\left((1 - T_{11}(E))S(E) - (T_{14}(E) + T_{12}(E))(T_{41}(E) + T_{21}(E))\right)$$

$$\alpha_{22}(E) = \frac{e^2}{hS(E)}\left((1 - T_{22}(E))S(E) - (T_{21}(E) + T_{23}(E))(T_{32}(E) + T_{12}(E))\right)$$

$$\alpha_{12}(E) = \frac{e^2}{hS(E)}\left((T_{12}(E)T_{34}(E) - T_{14}(E)T_{32}(E))\right)$$

$$\alpha_{21}(E) = \frac{e^2}{hS(E)}\left((T_{21}(E)T_{43}(E) - T_{41}(E)T_{23}(E))\right)$$

$$S(E) = T_{12}(E) + T_{14}(E) + T_{32}(E) + T_{34}(E). \quad (C.3)$$

References

[1] Landauer R 1970 *Philos. Mag.* **21** 8637
[2] Büttiker M 1986 *Phys. Rev. Lett.* **57** 17614
[3] Yacoby A, Heiblum M, Mahalu D, Umansky V and Shtrikman H 1995 *Phys. Rev. Lett.* **74** 4047-50
[4] Onsager L 1931 *Phys. Rev.* **38**, 2265-79
[5] Schuster R, Buks E, Heiblum M, Mahalu D, Umansky V and Shtrikman H 1997 *Nature* **385** 417-20
[6] Sigrist M, Fuhrer A, Ihn T, Ensslin K, Ulloa S E, Wegscheider W and Bichler M 2004 *Phys. Rev. Lett.* **93** 066802
[7] Gerland U, von Delft J, Costi T A and Oreg Y 2000 *Phys. Rev. Lett.* **84** 3710-13
[8] Yang Ji, Heiblum M, Sprinzak D, Mahalu D and Shtrikman H 2000 *Science* **290** 779-83
[9] Yang Ji, Heiblum M and Shtrikman H 2002 *Phys. Rev. Lett.* **88**, 076601
[10] Zaffalon M, Aveek Bid, Heiblum M, Mahalu D, Umansky V 2008 *Phys. Rev. Lett.* **100** 226601

[11] Takada S, Bäuerle C, Yamamoto M, Watanabe K, Hermelin S, Meunier T, Alex A, Weichselbaum A, von Delft J, Ludwig A, Wieck A D, Tarucha S 2014 *Phys. Rev. Lett.* **113** 126601

[12] Takada S, Yamamoto M, Bäuerle C, Alex A, von Delft J, Ludwig A, Wieck A D, Tarucha S 2016 *Phys. Rev. B* **94**, 081303(R)

[13] Avinun-Kalish M, Heiblum M, Zarchin O, Mahalu D and Umansky V 2005 *Nature* **436** 529-33

[14] Yeyati A L and Büttiker M 1995 *Phys. Rev. B* **52** R14360

[15] Lee H-W 1999 *Phys. Rev. Lett.* **82**, 2358-61

[16] Taniguchi T and Büttiker M 1999 *Phys. Rev. B* **60** 13814-23

[17] Yeyati A L and Büttiker M 2000 *Phys. Rev. B* **62** 7307-15

[18] Hackenbroich G, Heiss W D and Weidenmüller H A 1997 *Phys. Rev. Lett.* **79** 127-30

[19] Baltin R, Gefen Y, Hackenbroich G and Weidenmüller H A 1999 *Eur. Phys. J. B* **10** 119-29

[20] Silvestrov P G and Imry Y 2000 *Phys. Rev. Lett.* **85** 25658

[21] Silvestrov P G and Imry Y 2007 *New J. Phys.* **9** 125

[22] Goldstein M, Berkovits R, Gefen Y and Weidenmüller H A 2009 *Phys. Rev. B* **79** 125307

[23] Karrasch C, Hecht T, Weichselbaum A, Oreg Y, von Delft F and Meden V 2007 *Phys. Rev. Lett.* **98** 186802

[24] Silva A, Oreg Y and Gefen Y 2002 *Phys. Rev. B* **66** 195316

[25] Oreg Y 2007 *New J. Phys.* **9** 122

[26] Molina R A, Jalabert R A, Weinmann D and Jacquod P 2012 *Phys. Rev. Lett.* **108** 076803

[27] Molina R A, Schmitteckert P, Weinmann D, Jalabert R A and Jacquod P 2013 *Phys. Rev. B* **88** 045419

[28] Jalabert R A, Weick G, Weidenmüller H A and Weinmann D 2014 *Phys. Rev. E* **89** 052911

[29] Wu J, Gu B-L, Chen H, Duan W and Kawazoe Y 1998 *Phys. Rev. Lett.* **80** 19525

[30] Kang K 1999 *Phys. Rev. B* **59** 4608-11

[31] Aharony A, Entin-Wohlman O, Halperin B I and Imry Y 2002 *Phys. Rev. B* **66** 115311

[32] Entin-Wohlman O, Aharony A, Imry Y, Levinson Y and Schiller A 2002 *Phys. Rev. Lett.* **88** 166801

[33] Takada S, Yamamoto M, Bäuerle C, Watanabe K, Ludwig A, Wieck A D and Tarucha S 2015 *Appl. Phys. Lett.* **107** 063101

[34] Buchholz S S, Fischer S F, Kunze U, Reuter D and Wieck A D 2009 *Appl. Phys. Lett.* **94** 022107

[35] Kreisbeck C, Kramer T, Buchholz S S, Fischer S F, Kunze U, Reuter D and Wieck A D 2010 *Phys. Rev. B* **82** 165329

[36] Kramer T, Heller EJ and Parrott RE 2008 *J. Phys. Conf. Series.* **99** 012010

[37] Chaves A, Farias GA, Peeters FM and Szafran B 2009 *Phys. Rev. B* **80** 125331

[38] Kramer T, Kreisbeck C and Krueckl V 2010 *Phys. Scr.* **82** 038101

[39] Kramer T, Kreisbeck C, Riha C, Chiatti O, Buchholz S S, Wieck A D, Reuter D and Fischer S F 2016 *AIP Advances* **6** 065306

[40] Buchholz S S, Kunze U, Reuter D, Wieck A D and Fischer S F 2011 *App. Phys. Lett.* **98** 102111

[41] Baranger H U, DiVicenzo D P, Jalabert R A and Stone A D 1991 *Phys. Rev. B* **44** 10637-75

[42] Kobayashi K, Aikawa H, Katsumoto S and Iye Y 2002 *J. Phys. Soc. Jpn.* **71** 20947

[43] Ferry D K and Goodnick S M 1997 *Transport in nanostructures* (Cambridge University Press)

[44] Molina R A, Schmitteckert P, Weinmann D, Jalabert R A, Jacquod P 2012 *J. Phys.: Conf. Ser.* **338** 012011

[45] Kouwenhoven L P, Austing D G, Tarucha S 2001 *Rep. Prog. Phys.* **64** 701-36

[46] Tarucha S, Austing D G, Honda T, van der Hage R J, Kouwenhoven L P 1996 *Phys. Rev. Lett.* **77** 3613/-6

[47] Kouwenhoven L P, Marcus C M, McEuen P L, Tarucha S, Westervelt R M, Wingreen N S 1997 *Electron transport in quantum dots* on *Mesoscopic electron transport* (Kluwer)

[48] Babinski A, Potemski M, Raymond S, Lapointe J, Wasilewski Z R 2006 *Phys. Rev. B* **74** 155301

[49] Garashchuk S and Tannor D J 1998 *J. Chem. Phys.* **109** 3028-36

[50] Tannor D J and Garashchuk S 2000 *Annu. Rev. Phys. Chem.* **51** 553–600

[51] Feit M D, Fleck J A and Steiger A 1982 *J. Comp. Phys.* **47** 412-33